

Characterizing Urban Planetary Boundary Layer Dynamics Using 3-Year Doppler Wind Lidar Measurements in a Western Yangtze River Delta City, China

Tianwen Wei¹, Mengya Wang^{1,2*}, Kenan Wu¹, Jinlong Yuan¹, Haiyun Xia^{1,3*}, Simone Lolli⁴

¹School of Atmospheric Physics, Nanjing University of Information Science & Technology, Nanjing 210044, China.

²China Meteorological Administration Xiong'an Atmospheric Boundary Layer Key Laboratory, Xiong'an New Area, Baoding 071800, China

³School of Earth and Space Science, University of Science and Technology of China, Hefei 230026, China

⁴CNR-IMAA, Contrada S. Loja snc, Tito Scalo (PZ), 85050, Italy

Correspondence to: Mengya Wang (wmengya123@nuist.edu.cn) and Haiyun Xia (hsia@ustc.edu.cn)

Abstract

The planetary boundary layer (PBL) dynamics play a critical role in shaping urban atmospheric processes by governing the exchange of energy, momentum, and mass within the lower atmosphere. This study investigates PBL dynamics in Hefei, a city in the Western Yangtze River Delta, using three years (June 2019 to June 2022) of Doppler wind lidar data. Seasonal and diurnal variations in key parameters, including wind profiles, shear intensity, turbulent mixing, low-level jets (LLJs), and mixing layer heights (MLH), are analyzed. Results show that horizontal wind speeds accelerated more rapidly above 3 km, with the predominant westerly winds ($270^{\circ}\pm 15^{\circ}$) in all seasons. The vertical depth of high wind zone ($> 8 \text{ m s}^{-1}$) during the day is found generally deeper than at night, particularly in winter. In Hefei, LLJs primarily form at sunset and dissipate by noon, typically at altitudes between 0.5 and 0.6 km throughout the year, except in July. LLJ occurrences are most frequent in spring (31.7%), followed by summer (24.7%), autumn (22.3%), and winter (21.3%). Summer LLJs are most intensified, extending up to 1.5 km. The larger wind gradient below the jets significantly enhances turbulence and shear intensity near the ground at night. The seasonal average MLH peaks between 2:00 p.m. and 3:00 p.m., reaching approximately 1.2 km in spring and summer. Cloud cover raises MLH by about 100 m at night but decreases it by 200 m at the afternoon peak. This study provides insights into lidar-based PBL dynamics and highlights implications for local standards concerning low-altitude economic activities.

1. Introduction

The planetary boundary layer (PBL) refers to the lowest 1~3 km of the atmosphere that is directly influenced by the presence of the underlying surface, and typically responds to surface forcings in an hour or less (Stull, 1988). These surface forcings include frictional drag, heat exchange, pollutant emission, evaporation and transpiration, and terrain induced flow modifications (Garratt, 1994). The depth and structure of the PBL are determined by the physical and thermal properties of the underlying

38 surface as well as the dynamics and thermodynamics of the lower atmosphere (Madala et al., 2014;
39 Barlow, 2014). One of the most important characteristic of the PBL is turbulence, which dominates the
40 vertical exchange of heat, moisture, momentum, trace gases, and aerosols between the free atmosphere
41 and the Earth's surface or regolith (Baklanov et al., 2011; Petrosyan et al., 2011). In the PBL, the sources
42 of turbulent mixing exhibit significant temporal and spatial variations, which include buoyancy
43 (convective mixing), wind shear (mechanical mixing), entrainment at the top of boundary layer, and
44 radiative cooling in stratocumulus clouds (top-down convective mixing) (Ortiz-Amezcuca et al., 2022).
45 Such turbulent motion in the PBL has been demonstrated to be inherently connected to air pollution by
46 modulating the dispersion, transport, and accumulation process, and have critical impacts on land-
47 atmosphere energy balance, as well as aerosol-cloud-precipitation-radiation interactions (Kim and
48 Entekhabi, 1998; Wang et al., 2001; Chen et al., 2011; Wood et al., 2015; Li et al., 2017; Su et al., 2020,
49 2018; Pérez-Ramírez et al., 2019, 2021; Christensen et al., 2024).

50 Hefei, the capital of Anhui province, has experienced incredible economic growth and urban sprawl
51 over the past two decades (Zhao and Zou, 2018). Situated between the Yangtze River and Huaihe River,
52 in what is known as the Jianghuai region, the Hefei Metropolitan Circle plays a pivotal role in the Yangtze
53 River-Huaihe River Water Transfer Project to provide benefits for water supply, transportation,
54 agriculture, and power generation (Li et al., 2019; Zhang et al., 2023). Apart from tremendous economic
55 benefits achieved in Hefei, intense human activities create a profound influence on the local climate,
56 affecting the thermal, hydrological, and wind environments in the PBL within and beyond city limits (Shi
57 et al., 2008; Li et al., 2022a). In this context, the PBL study is vital for better understanding the exchange
58 process between the atmosphere and land over complex underlying surfaces, and improving the
59 parameterization schemes in numerical weather prediction models. However, previous studies mainly
60 focused on surface air pollution characteristics and its associations with meteorological parameters, as
61 well as the impacts on human health based on in-situ monitoring measurements or air quality modelling
62 (Hu et al., 2024; Qin et al., 2017; Shen et al., 2022; Zhang et al., 2017; Zhu et al., 2019). Among various
63 observation techniques, the lidar is a powerful tool and has been applied in retrieve vertical profiles of
64 PBL properties, such as aerosols, winds, turbulence, precipitation, temperature, and water vapor during
65 a period (Zhou, 2002; Xia et al., 2015, 2016; Wei et al., 2021, 2022, 2025; Jiang et al., 2022; Yuan et al.,
66 2020; Wang et al., 2015b). Therefore, it is essential to utilize the long-term lidar measurement to
67 characterize the PBL dynamics such as winds and turbulence sources to further understand the land-
68 atmosphere interaction.

69 The key parameter of PBL meteorology is the PBL height (PBLH) which displays significant
70 spatiotemporal variability under different atmospheric and surface conditions (Guo et al., 2019; Zhang
71 et al., 2022; Zhao et al., 2023). It strongly depends on surface characteristics such as surface heating rate,
72 strength of winds, topography, surface roughness, free atmospheric characteristics, the amount of clouds
73 and moisture (Kotthaus et al., 2023; Zhang et al., 2020). Multiple approaches have been developed to
74 determine the PBLH based on observations, such as in situ radiosonde (Gu et al., 2022; Guo et al., 2021;
75 Yue et al., 2021), aerosol-based and dynamic-based lidar techniques (Chen et al., 2022; Huang et al.,
76 2017; Vivone et al., 2021; Wang et al., 2020, 2021; Yang et al., 2020; Yin et al., 2019). In the practical
77 measurements of PBLH, it is necessary to consider its distinct diurnal cycle of PBL. The PBL can be
78 categorized into three dominant regimes: convective boundary layer (CBL), stable boundary layer (SBL),
79 and residual layer (RL) based on the thermodynamic stability in the lower atmosphere (Caughey and
80 Palmer, 1979). After sunrise, increasing radiative heating triggers the development of near-surface
81 turbulent eddies and leads to the formation of CBL, which grows with time and reaches its maximum in

82 the early afternoon. The CBL consists of a convective surface layer, mixing layer (ML) above, and
83 entrainment zone (EZ) at the top (Wyngaard, 1988). After sunset, the radiative cooling creates the SBL
84 close to the surface and its depth grows as night progresses. The RL lies above the SBL meanwhile a
85 capping inversion overlies the RL (Fochesatto et al., 2001). However, studies in diurnal and seasonal
86 characteristics of the PBLH under different stable conditions in Hefei based on long-term measurements
87 have not been documented yet, to the best of our knowledge at the writing of this work.

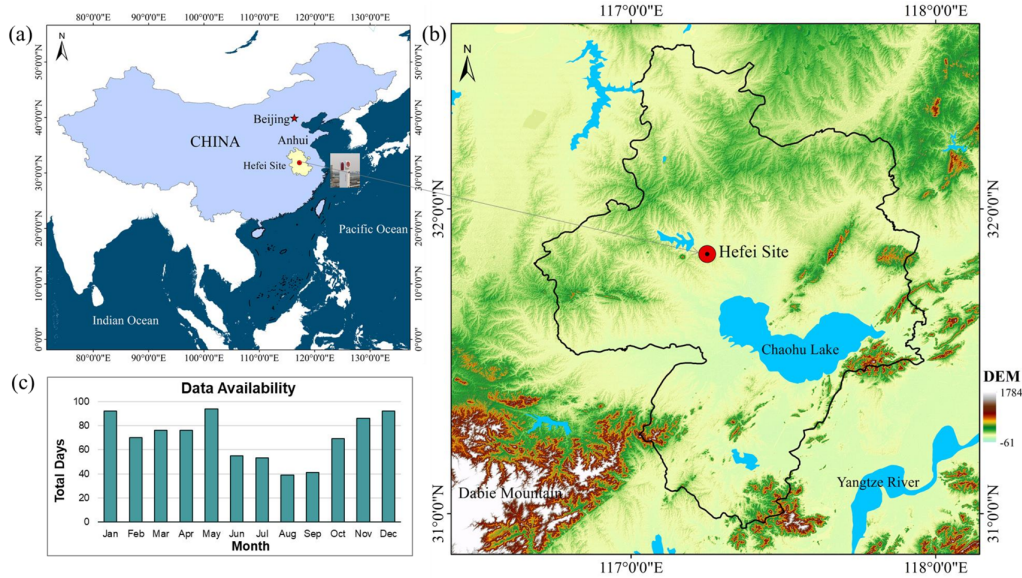
88 Turbulence in the PBL is generated mechanically by wind shear, and convectively by buoyancy.
89 Wind shear is the main source of turbulence in the nocturnal boundary layer (NBL, also known as the
90 SBL), which can be enhanced in the presence of low-level jets (LLJs). Yang et al. (2023) found that wind
91 shears induced by LLJs often enhanced the vertical mixing processes, reduced the atmospheric stability,
92 and resulted in small weak direction shifts in eastern Idaho, USA. The formation of LLJ can provide a
93 driving force for the development of a deeper CBL on the Tibet Plateau (Su et al., 2024). Many studies
94 investigated the prominent role of LLJs in heavy rainfall events in the Jianghuai region (Chen et al., 2020;
95 Yan et al., 2021; Liu et al., 2022; Cui et al., 2023), but there has been a lack of research specifically
96 focusing on Hefei. The Huaihe River region, including Hefei, is one of the six high-frequency regions of
97 LLJs in China (Yan et al., 2021). The LLJs over China are usually classified into two types: boundary
98 layer jets (BLJs, below 1 km) and synoptic-system-related LLJs (SLLJs, within 1–4 km) (Du et al., 2014).
99 The occurrence of BLJs is associated with significant vertical shear of horizontal wind and diurnal
100 variation. On the contrary, SLLJs are usually related to synoptic-scale weather systems. This study
101 addresses a previous research gap by investigating the characteristics of LLJs formation and types, and
102 vertical wind shear (VWSH) in Hefei, with a focus on their monthly variations across different times and
103 altitudes.

104 In this paper, we utilize 3-year Doppler wind lidar measurements to characterize the PBL dynamics
105 in Hefei. The horizontal wind speeds and direction, LLJs, VWSH, turbulent kinetic energy dissipation
106 rate (TKEDR), mixing layer height (MLH) and PBLH are thoroughly analyzed. Remote sensing retrieval
107 of the above PBL parameters have been fully illustrated and validated in our previous studies (Wang et
108 al., 2019, 2021; Wei et al., 2019, 2022; Wang et al., 2024). This paper aims to shed new light on the
109 diurnal and seasonal characteristics of PBL meteorology and turbulence influenced by diurnal cycles,
110 general circulation, the Asian monsoon, and the synoptic systems.

111 **2. Materials and methodology**

112 **2.1 Study area and instruments**

113 Hefei, a rapidly developing new first-tier city, is located in Eastern China within central Anhui
114 Province in Figure 1(a). It covers an area of 11465 km², comprising four urban districts, one county-level
115 Chaohu city, and four counties. Its topography includes flat plains, gently rolling hills, and major water
116 bodies such as Chaohu Lake to the southeast in Figure 1(b). The city altitude mainly ranges from 15 to
117 81 m, with the highest point reaching 595 m (Sun and Ongsomwang, 2021). The Dabie Mountain in the
118 southwest introduces varied elevations and complex topographical features that influence regional
119 atmospheric dynamics in Hefei. Anhui province including Hefei, is located across both the eastern
120 monsoon region and the north-south climate transition zone of China. Hence, Hefei is characterized by
121 the typical subtropical monsoon climate with four distinct seasons. The city receives an annual
122 precipitation of ~1000 mm and average temperature of 15.7 °C, with prevailing southeast winds in spring
123 and summer and northwest winds in autumn and winter (Li et al., 2024).



124

125

126

127

128

Figure 1. Study area and location of the Doppler wind lidar system. (a) Location (31.83°N, 117.25°E) of Hefei site and administrative boundary of Anhui province; (b) Digital Elevation Model (DEM), showing topographical features with the solid black line representing the administrative boundary of Hefei city; (c) Data availability of 3-year Doppler wind lidar measurements. Total days with valid lidar measurements are accounted for each month.

129

Table 1. Key operating parameters of the Doppler lidar system

Parameter	Value
Wavelength (nm)	1548
Pulse energy (μ J)	300
Pulse duration (ns)	600
Repetition rate (kHz)	10
AOM frequency shift (MHz)	80
Diameter (mm)	100
Sampling frequency (MHz)	250
Range gate length (m)	30/60/150
Radial time resolution (s)	1
Scanning mode	VAD
Elevation angle ($^{\circ}$)	60
Azimuth angle ($^{\circ}$)	0-300

130

131

132

133

134

135

136

137

138

139

140

141

142

143

A compact coherent Doppler wind lidar (CDWL) system was deployed on the roof of the School of Earth and Space Science (SESS) building of the University of Science and Technology of China (31.83° N, 117.25°E) in the urban area of Hefei, to monitor the vertical profiles of aerosol, cloud and wind field. The lidar location is denoted as the Hefei site in Figures 1(a) and 1(b). The lidar system operates at 1.5 μ m eye-safe wavelength and uses 300 μ J pulse energy and 10 kHz repetition rate to achieve a maximum detection range of up to 15 km. During the long-term experiment, the lidar performed continuous velocity azimuth display (VAD) scanning mode for high spatial-temporal resolution wind profile measurement. The azimuth angle ranges from 0° to 300° with an interval of 5° and the elevation angle is 60°. The key operating parameters of the Doppler lidar system are summarized in Table 1. Detailed information about the validation and application of the lidar system can be found in our previous works (Jia et al., 2019; Wei et al., 2020, 2021). The data availability is presented in Figure 1(c) with monthly statistics of total valid days. Note that the lower data availability during the summer seasons is primarily due to frequent rainfall and high temperatures, which caused instability in the lidar systems. However, these issues have

144 been significantly improved in the recently updated systems (Xia et al., 2024).

145 2.2 Datasets and methods

146 The CDWL system operated for three consecutive years from June, 2019 to June, 2022, except for
147 some maintenance interruptions (Wang et al., 2024). Table 2 presents the number of available observation
148 days for each season and weather type.

149 **Table 2.** Observation days by weather type during Doppler lidar operations

Weather Types*	Spring	Summer	Autumn	Winter	Total days
Rainy	62	44	37	75	218
Clear	69	21	47	76	213
Cloudy	68	82	50	64	264
Partly Cloudy	39	38	44	39	160

150 ***Rainy:** rain persists for more than 2 hours **Clear:** clouds are present for less than 2 hours.

151

Cloudy: cloud coverage exceeds 8 hours. **Partly Cloudy:** cloud coverage lasts between 2 to 8 hours.

152 The time resolution and range gate resolution of the original radial measurements are 1 s and 30 m,
153 respectively. Horizontal wind speed (HWS), horizontal wind direction (HWD), and vertical wind speed
154 (VWS) are retrieved from the measured radial speeds at different azimuth angles using a filtered sin-
155 wave fitting method, based on the assumption of horizontally homogenous wind field (Smalikho, 2003;
156 Banakh et al., 2010; Wei et al., 2020). Considering the duration of one VAD scan, the time resolution of
157 wind profile becomes about 2 minutes. Here, the wind direction of 0° represents the horizontal wind
158 coming from the north, and the angle increases clockwise. The negative (positive) vertical wind speed
159 was defined as upward (downward) motion in this study.

160 Turbulence activity can be expressed by vertical velocity variance, spectrum width, turbulent kinetic
161 energy, and TKEDR (O'Connor et al., 2010). In this study, we estimate TKEDR using the turbulence
162 statistical model based on the relation between the structure-function of the measured radial velocity and
163 theoretical value (Banakh et al., 2017). The MLH is a significant parameter for presenting the vertical
164 turbulent exchange within the PBL. On the basis of the characteristics of decreasing convective
165 turbulence intensity along with height, the threshold method can effectively determine a typical
166 turbulence height. Here, the MLH is defined as the height up to which $\text{TKEDR} > 10^{-4} \text{ m}^2 \text{ s}^{-3}$ is reached
167 (Banakh et al., 2021; Wang et al., 2021). In addition, the aerosol-based PBLH, shown in Section 3.6, is
168 also calculated for comparison. It is determined from the aerosol backscatter coefficient using a Harr
169 wavelet method (Caicedo et al., 2017; Kotthaus et al., 2023).

170 LLJ is a fast air stream with a wind speed maximum in the lowest kilometers of the troposphere
171 (Stull, 1988). Referring the previous studies (Qiu et al., 2023; Zhang et al., 2018; Tuononen et al., 2017)
172 and considering the local characteristics, we identify the LLJs at Hefei using the following criteria: (1)
173 the maximum wind speed $U_{max} > 8 \text{ m s}^{-1}$ and, (2) the wind speed difference $\Delta U = U_{max} - U_{min} >$
174 2.6 m s^{-1} , where U_{min} is the minimum wind speed above the height of U_{max} . The LLJ height is then
175 defined as the height of U_{max} . In addition, when a two-layer LLJ exists, the lower one will be selected.
176 Each wind profile was applied to identify the LLJ event. In the statistics procedure of Section 3.3, a time
177 window of 1 h is used to filter out the outliers, and those with fewer than 60% within the window were
178 abandoned.

179 Vertical wind shear (VWSH) is defined as the change in wind speed and/or direction with height. It
180 can be calculated from the vertical wind profiles using the following equation (Manninen et al., 2018)

181

$$VWSH = \frac{(\Delta u^2 + \Delta v^2)^{0.5}}{\Delta z}$$

182

where the difference in vectors of the wind components u and v is divided by the height difference Δz

183

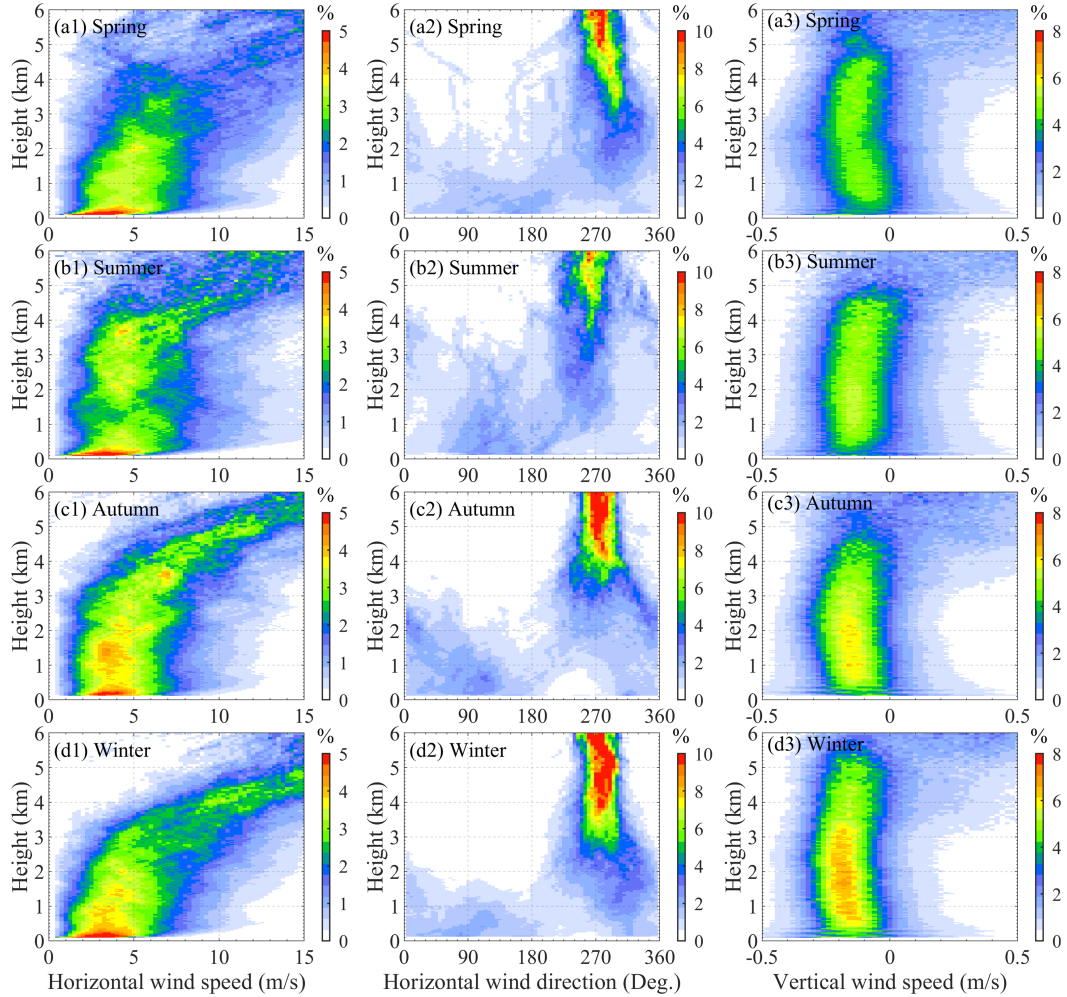
between the two altitude levels used to compute the wind shear.

184

3. Results

185

3.1 The 3-year seasonal profiles of the wind frequency



186

187

Figure 2. Seasonal frequency distributions of (a1-d1) horizontal wind speed, (a2-d2) horizontal wind direction, and

188

(a3-d3) vertical wind speed below 6 km in Hefei. Panels (a-d) represent spring (Mar-May), summer (Jun-Aug),

189

autumn (Sep-Nov), and winter (Dec-Feb), respectively. Frequencies along the x-axis are normalized to 100% at each

190

height. Negative vertical wind speeds indicate upward motion.

191

Vertical wind profiles are influenced by surface friction, terrain, local pressure systems, and global

192

atmospheric circulation patterns. We retrieve the vertical profiles of HWS, HWD, and VWS and calculate

193

the frequency (%) of their occurrence at different heights above ground level (AGL), as shown in Figure

194

2. The frequency distribution represents the ratio of wind speeds within each x-axis bin to the total valid

195

counts at a given height. Therefore, the sum of all frequency values along the x-axis is 100% at any

196

specific height. To represent rich details, the bin size or resolution (i.e., the width of each column) is set

197

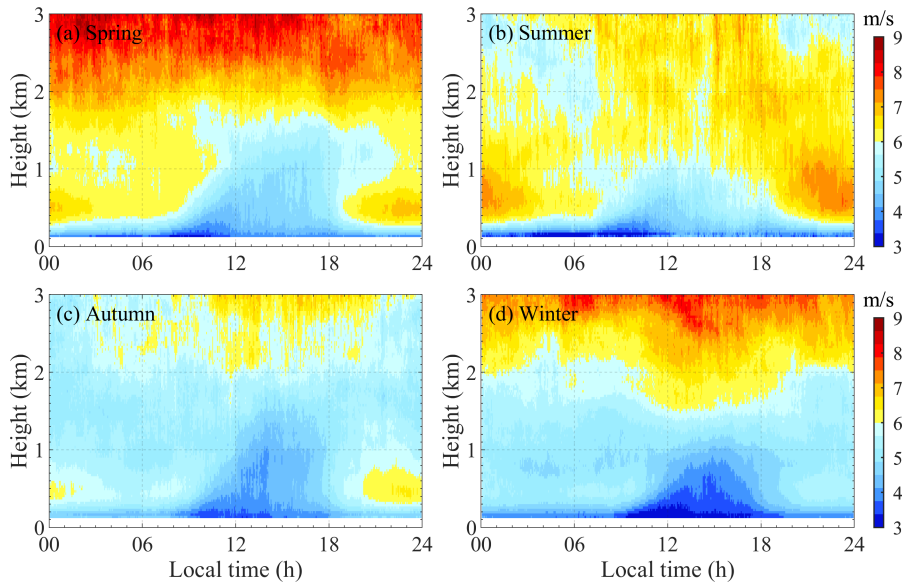
to 0.25 m s^{-1} , 5° , and 0.02 m s^{-1} for HWS, HWD, and VWS, respectively.

198 In the left panel of Figure 2, the frequency distribution of HWS (hereafter referred to as HWS%)
199 exhibits a rightward skew in all seasons, a characteristic often modeled using a Weibull or Lognormal
200 distribution due to the non-negative nature of wind speed (Justus et al., 1978; Pobočková et al., 2017).
201 Close to the ground, the majority of HWS values are clustered at the lower end, mainly as a result of
202 surface friction. Below ~300 m AGL, HWS increases rapidly as surface friction decreases. From 300 m
203 to 3 km AGL, HWS increases steadily while becoming more dispersed, with the overall distribution
204 (HWS%) spanning between 2 and 7 m s⁻¹. Above 3 km, HWS accelerates more rapidly, particularly in
205 autumn and winter, where HWS% remains relatively concentrated. In contrast, HWS% in spring and
206 summer is more dispersed with a lower frequency of high HWS occurrences (> 10 m s⁻¹). Many studies
207 have demonstrated a significant decrease trend of near surface wind speed in eastern China including
208 Anhui province, induced by large-scale circulation and local land use and land cover change (Li et al.,
209 2018; Liu et al., 2023; Li et al., 2022). Wang et al. (2015) observed that the value of annual mean surface
210 wind speed in Hefei city during 1981-2012 was between 2.0 m s⁻¹ and 2.6 m s⁻¹ and the highest frequency
211 of maximum surface wind speed occurred in spring. A recent study by Li et al. (2022a) analyzed the
212 maximum daily wind speed of 10 minutes from 51 meteorological stations in Anhui province from 2006
213 to 2020, which showed that the average maximum wind speed in the city of Hefei was between 9.1~17.6
214 m s⁻¹. Therefore, our results of seasonal HWS values near the ground correspond to previous studies.

215 The frequency distribution of HWD (hereafter referred to as HWD%) exhibits distinct vertical
216 characteristics, as shown in the middle panel of Figure 2. At higher altitudes (> 3 km), the distribution of
217 HWD is much more concentrated, with predominant westerly winds (270°±15°) in all seasons. Because
218 Hefei city is located between 31°4' N and 32°38' N, which is affected by westerly circulation. The finding
219 of prevailing westerlies throughout the year in Hefei is consistent with (Sun et al., 2021). In contrast, the
220 influence of westerly on HWD% below the PBL is insignificant due to the impact of the underlying
221 surface roughness, terrain distribution, and air flow turbulence. Below 3 km AGL, we can discover
222 notable southwest winds in summer compared to the other seasons. In the summer monsoon season,
223 eastern China (including Hefei city) is mainly dominated by southwest winds, as has been reported by
224 many studies (Liu et al., 2015; Yan et al., 2022; Zhao et al., 2007). Wind directions in the PBL tend to be
225 more variable and chaotic compared to those at higher altitudes. And westerly winds above 1.5 km
226 consistently strengthen with increasing altitude in all seasons.

227 The right panel of Figure 2 illustrates seasonal profiles of VWS frequency (hereafter referred to as
228 VWS%). The frequency distribution of VWS% is right-skewed and its center lay in negative values
229 between -0.2 m s⁻¹ and -0.1 m s⁻¹. The results show that most VWS values are negative below 5 km in all
230 seasons, representing upward motion in the atmosphere. It demonstrates the asymmetric nature of vertical
231 velocities in the atmosphere, where upward movements are stronger than downward movements
232 (Tamarin-Brodsky and Hadas, 2019). Furthermore, Figure 2 (d3) shows that winter has the highest
233 frequency of negative VWS, with most VWS% ranging from 4% to 7% below 3 km AGL. A climatology
234 study of cold frequency suggests that cold fronts are most frequently occurred in cold seasons over Hefei
235 city (Xue et al., 2022). In winter, cold fronts associated with the winter monsoon can enhance upward
236 motion of the air as the heavier (more dense) cool air pushes under the lighter (less dense) warm air
237 (Kang et al., 2019; Parsons, 1992). The upward motion intensifies and is vigorous along the frontal
238 boundaries, leading to cloud formation and precipitation. The higher positive values in the asymmetric
239 distribution of VWS, particularly above 3 km, are attributed to the contribution of falling precipitation
240 particles (Wei et al., 2019). Under these conditions, the detected vertical speed reflects the movement of
241 larger hydrometeors rather than the air motion itself.

242 **3.2 Diurnal HWS profiles in different seasons**



243
 244 **Figure 3.** Time-height diagrams of seasonal average horizontal wind speed profiles below 3 km. (a) Spring: Mar-
 245 May; (b) Summer: Jun-Aug; (c) Autumn: Sep-Nov; and (d) Winter: Dec-Feb.

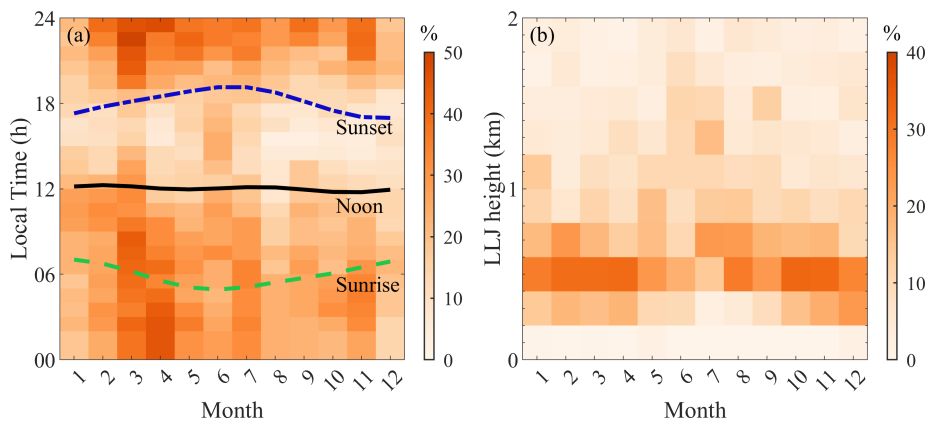
246 The diurnal variation of the vertical wind profile within the PBL is intricately linked to the dynamics
 247 and thermodynamics driven by the daily cycle of solar heating and longwave cooling. Figure 3 illustrates
 248 how HWS profile varies with local time (LT) on a seasonal scale. Minimum HWS values are observed
 249 near the surface due to the influence of surface roughness.

250 During the day, solar heating induces turbulence and convection, which increases surface friction
 251 and slows down the up-level horizontal wind. This results in the formation of a gentle wind zone (GWZ),
 252 characterized by wind speeds below 5 m s^{-1} , a feature that can be observed in all seasons. And the diurnal
 253 variation of the GWZ strongly correlates with the development of the mixing layer. At night, radiative
 254 cooling generates a temperature inversion, inhibiting vertical mixing and fostering laminar flow with
 255 increased shear intensity. Consequently, nocturnal winds are generally stronger than daytime winds at
 256 the same height below 1.5 km AGL throughout all seasons. Above this height, the HWS profile is usually
 257 more uniform and stronger due to the reduced frictional drag in the free atmosphere. It is interesting to
 258 find that the vertical height of high wind zone ($> 8 \text{ m s}^{-1}$) during the day is much lower than at night,
 259 particularly in winter. In Figure 3d, an appreciable enhancement of HWS at 1.5 km is discovered during
 260 the day particularly between 11:00 a.m. and 16:00 p.m., when the PBL tends to grow and become deeper
 261 due to radiative heating of the surface. In general, the HWS increases with height. However, as seen in
 262 Figures 3(a) to 3(c), a distinct local maximum in HWS, occurring between approximately 0.4 km and 0.8
 263 km, is observed after 8:00 p.m. and before 7:00 a.m. the next day. This is especially pronounced in
 264 summer, where the highest values and the highest vertical extent of the wind are recorded. These winds
 265 are typically associated with the nocturnal LLJs, a narrow band of strong winds that forms in the lower
 266 PBL. Although the seasonal average HWS reflects the overall wind conditions, the pronounced notch
 267 structure in the profile underscores the frequent occurrence of LLJs, which will be explored in more
 268 detail in the next section.

269 **3.3 Monthly characteristics of LLJ at different times and heights**

270 LLJ is characterized by a concentrated band of strong winds located in the lower part of the

271 atmosphere. The diurnal variation of its formation and occurrence is influenced by the interaction
 272 between surface heating/cooling cycles, atmospheric stability, and synoptic-scale weather patterns.
 273 Figure 4(a) illustrates the statistical frequency (%) of the occurrences of LLJs at different hours for each
 274 month. Frequency values are calculated as the ratio of the total number of LLJ occurrences to the total
 275 number of available days in the specific month over a 3-year period. Additionally, the monthly variation
 276 of the sunrise, noon, and sunset time was also plotted. Figure 4(b) presents the frequency distribution (%)
 277 of LLJs occurrences over the height for each month, with the sum of each column equaling 100%. The
 278 seasonal wind rose charts of the LLJ events are presented in Figure 5(a)~(d). The seasonal and
 279 intraseasonal variability of predominant wind directions and wind speeds of LLJs are influenced by
 280 general circulation, the East Asian monsoon, and synoptic systems.



281
 282 **Figure 4.** (a) Monthly frequency (%) of LLJ occurrences over time. The blue dot-dashed line indicates the mean
 283 sunset time, the black solid line marks noon, and the green long-dashed line represents sunrise. (b) Height
 284 distribution of LLJ occurrence frequency by month, with normalized column totals (100%).

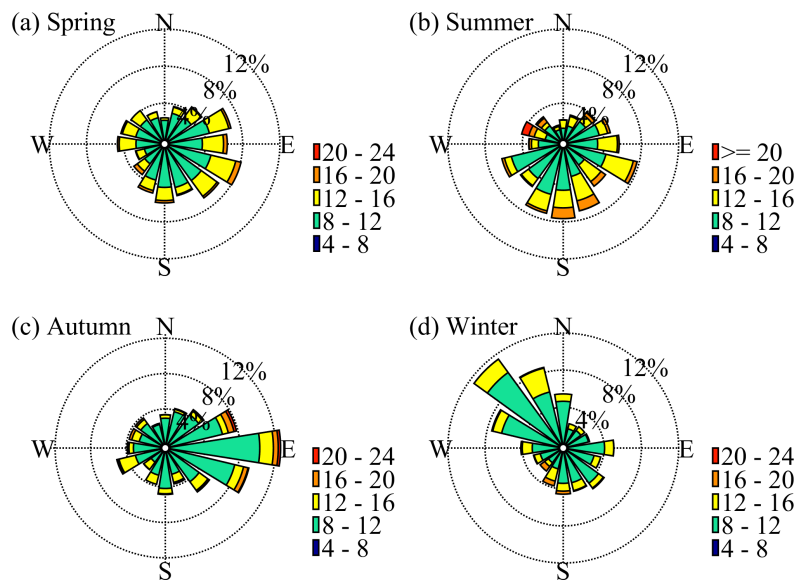
285 As shown in Figure 4(a), the results indicate that LLJs occur most frequently in spring in Hefei,
 286 which aligns with findings by Yan et al. (2021) based on long-term radiosonde observations in the Huaihe
 287 River Basin from 2011 to 2017. The seasonal average frequency of LLJ occurrences is highest in spring
 288 (31.7%), followed by summer (24.7%), autumn (22.3%), and winter (21.3%). LLJs are predominantly
 289 observed during the night and early morning throughout the year. According the classical theoretical
 290 description of inertial oscillations, nocturnal LLJs (NLLJs) form due to the decoupling of nocturnal
 291 winds from surface friction, facilitated by the development of a near-surface temperature inversion
 292 (Blackadar, 1957). At night, the ground cools more rapidly than the air above, giving a rise to the
 293 formation of temperature inversions. This inversion effectively reduces the influence of surface frictional
 294 on the air above it (Mirza et al., 2024). The reduced friction allows the wind aloft to accelerate, leading
 295 to the development of a pronounced super-geostrophic wind speed maximum. Such undisturbed inertial
 296 oscillations are widely recognized as a primary mechanism for the formation of NLLJ (Sisterson and
 297 Frenzen, 1978). LLJs are typically most pronounced during the early morning hours, just before the onset
 298 of daytime heating, when the temperature inversion is strongest due to prolonged nocturnal cooling. After
 299 sunrise, daytime heating gradually disrupts the stable boundary layer, reducing the conditions favorable
 300 for LLJ formation. Consequently, LLJs are less frequent between noon and sunset.

301 Figure 4(b) shows that more than 70% of LLJs occur at heights ranging from 0.3 km to 0.8 km AGL
 302 in all seasons except summer. The vertical distribution agrees with previous studies. For instance, Yan et
 303 al. (2021) reported that 400 m AGL was the most frequent height for the jet-nose appearing in the Huaihe
 304 River Basin. Wei et al. (2013) revealed that 76% of the observed LLJs occurred at an average altitude

305 below 600 m in the Yangtze River Delta region. Following the classification of Rife et al. (2010), the
 306 dominant type of LLJs in Hefei can be identified as BLJs that occur mainly in the PBL below 1 km AGL.
 307 The highest occurrence frequency of LLJs appeared between 0.5 km and 0.6 km AGL in most months,
 308 with peak heights between 0.7 and 0.8 km AGL in July.

309 The frequent occurrence of LLJs at heights below 1 km AGL enhances vertical mixing and
 310 turbulence within the lower atmosphere, breaking the decoupled boundary layer structure and restoring
 311 vertical heat, momentum, and pollutant exchanges. During nighttime, when stable stratification
 312 dominates, LLJs can reduce the accumulation of air pollutants near the surface by transporting them to
 313 higher altitudes. This mechanism is particularly important for urban areas like Hefei, where industrial
 314 and vehicular emissions often lead to air quality concerns. The temporal and vertical distribution of LLJs
 315 also has practical implications for low-altitude economic activities. For example, understanding LLJ
 316 dynamics provides valuable insights for designing safe and efficient drone flight routes, especially in
 317 areas with complex terrain or during nighttime operations. Additionally, the strong wind velocities
 318 associated with LLJs make them a key consideration for wind energy planning, particularly in optimizing
 319 the placement of wind turbines to maximize energy capture and efficiency.

320 The mechanisms driving LLJs include inertial oscillations under stable stratification, fronts and
 321 baroclinic weather patterns in flat terrain, orographic and thermal effects in complex terrain. Considering
 322 the topography and weather patterns, Hefei is prone to cyclones throughout the year, so the Asian
 323 monsoon system and synoptic processes may be the most important influential factors in LLJs activities.
 324 In contrast, previous studies on the LLJ climatology over other typical regions or cities showed different
 325 seasonal variations of LLJs occurrences. For example, LLJs occur more often in spring and winter in
 326 Beijing while those appear more frequently from October to December and from February to April in
 327 Guangzhou using long-term wind profiler observations (Miao et al., 2018).



328

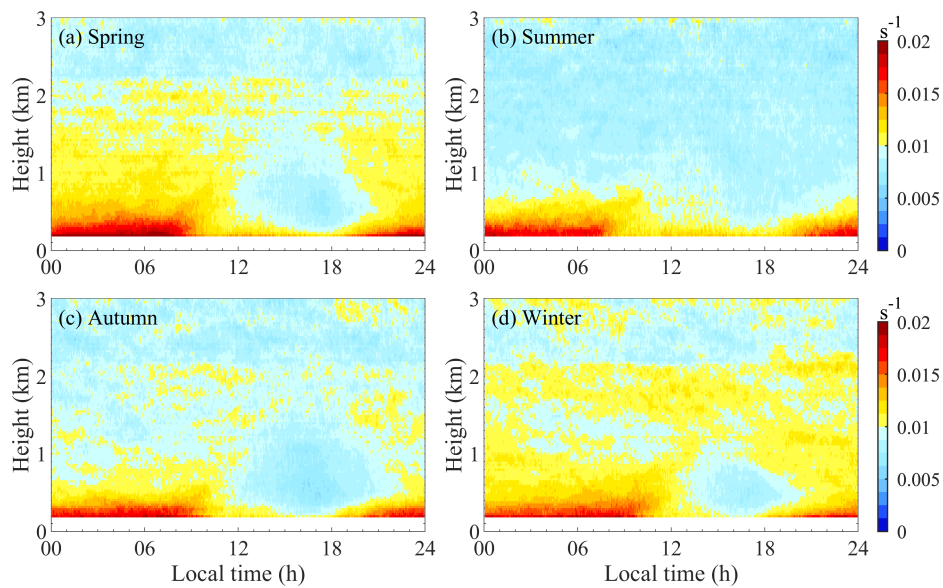
329

Figure 5. Seasonal wind rose diagrams of LLJ events at nose height at Hefei.

330 Figure 5 shows the wind characteristics at the nose height of LLJs across different seasons. The
 331 dominant wind directions are southeast in spring, south in summer, and more concentrated in autumn
 332 (easterly) and winter (northwesterly). These characteristics in Hefei are closely related to the East Asian
 333 monsoon system and associated large-scale atmospheric circulations. In spring, LLJs occur most
 334 frequently due to the interaction between cold northerly air masses and warm, moist southerly flows

335 during the transition from the East Asian Winter Monsoon (EAWM) to the East Asian Summer Monsoon
 336 (EASM). This dynamic interaction generates strong baroclinic conditions that are favorable for LLJ
 337 formation. In summer, the fully developed EASM and the northwestward expansion of the Western
 338 Pacific Subtropical High (WPSH)(Wang et al., 2023; Yang et al., 2022) stabilize the boundary layer
 339 structure, leading to fewer LLJs compared to spring but with greater intensity (more than half of HWS
 340 exceeding 12 m s^{-1}). The predominant wind directions during summer are southerly or southeasterly,
 341 reflecting the influence of the monsoonal flow. During autumn and winter, LLJs are less frequent as the
 342 WPSH retreats and the EAWM becomes dominant. Autumn marks the gradual transition, with occasional
 343 easterly LLJs influenced by the lingering WPSH. In winter, the stable conditions induced by the EAWM
 344 and associated high-pressure systems suppress LLJ formation, resulting in weak and infrequent
 345 northwesterly LLJs.

346 3.4 Diurnal cycle of VWSH profiles for each season



347

348

Figure 6. The same as in Fig. 3 but for VWSH.

349

VWSH depends directly on vertical wind profiles and exhibits both diurnal and seasonal variations within the boundary layer, as shown in Figure 6(a)~(d). Due to surface friction, the wind speeds decrease within the urban canopy, eventually reaching zero at ground level. These rapid changes in wind speed create a large wind speed gradient, resulting in an increased shear intensity in the surface layer. Throughout all seasons in Hefei, high VWSH values exceeding 0.015 m s^{-1} per meter (hereafter denoted by s^{-1}) are typically observed below 0.4 km.

355

Below 0.5 km, VWSH decreases from sunrise to the afternoon due to surface heating and increased atmospheric mixing, which consequently led to a more uniform wind profile (Figure 3). In contrast, it increases from sunset to early morning as surface cooling induces a temperature inversion, which creates a stable boundary layer where winds aloft decouple from the surface. At night, a sharper wind speed gradient with height is created under fully developed stable boundary layer, leading to maximum VWSH in this layer. In the low to mid-level atmosphere (0.5~1 km), VWSH also varies diurnally, with relatively lower values compared to VWSH below 0.5 km. Daytime VWSH in this layer is generally due to the well-mixed boundary layer. But it can vary depending on local weather conditions and synoptic influences. At night, high VWSH values above 0.01 s^{-1} is usually associated with the presence of a LLJ

363

364 and/or a strong temperature inversion, with the maximum VWSH typically occurring just below the core
365 of the LLJ. In the upper level (> 1 km), VWSH is less influenced by the diurnal cycle and remained
366 relatively stable throughout the day. However, high VWSH can still occur in this layer when it is coupled
367 with LLJs or influenced by large-scale synoptic systems.

368 The seasonal variation of VWSH is closely linked to the region's climatic patterns, particularly the
369 influence of the East Asian monsoons, which drive significant changes in temperature, wind patterns,
370 and atmospheric stability throughout the year. In general, high VWSH values (> 0.015 s⁻¹) near the
371 surface are related to LLJs occurrences across all seasons. On the contrary, VWSH values above 1 km in
372 spring and winter are significantly larger compared to summer and autumn, which spatial pattern also
373 corresponds to vertical distributions of seasonal HWS profiles. During the two seasons, Hefei often
374 receives invasion of cold air/surge events, leading to strong winds. In winter, Hefei experiences strong
375 VWSH primarily due to the impact of the EAWM and large-scale synoptic systems, such as cold fronts
376 and jet-streams. Weaker solar heating in winter results in less pronounced diurnal variation of VWSH.
377 These synoptic systems also lead to significant VWSH (> 0.01 s⁻¹) above 1 km, which is characterized
378 by strong winds aloft. In spring, Hefei experiences strong VWSH due to the transitional atmospheric
379 conditions of the season. The diurnal variation shows a decrease in VWSH after 8:00 a.m. in the morning
380 compared to winter (Figure 6a). The variability in wind directions and speeds contributed to fluctuating
381 VWSH above 1 km influenced by shifting synoptic-scale systems and developing convective activity in
382 late spring.

383 In contrast, relatively lower VWSH values between 0.005 s⁻¹ and 0.01 s⁻¹ above 1 km are observed
384 in summer. The weather is dominated by the summer monsoon flow and localized convective systems.
385 These conditions result in a generally weaker VWSH with less pronounced diurnal variation compared
386 to other seasons. Due to significant vertical convective mixing, the wind profile becomes more uniform,
387 resulting in weaker VWSH above 1 km (Figure 6b). As the influence of the winter monsoon begins to
388 dominate, the strong winds aloft and weak surface winds contribute to an increasing VWSH in autumn
389 compared to summer (Figure 6c). Similar to winter, VWSH in autumn is more pronounced at night and
390 early morning due to the formation of temperature inversions. During the day, the reduction in VWSH
391 driven by vertical mixing is less noticeable than in summer, as the overall atmospheric stability increases.

392 **3.5 Seasonal characteristics of the diurnal TKEDR profiles**

393 As one of the characteristic features of atmospheric turbulence, the TKEDR plays a crucial role in
394 boundary layer parameterization schemes. It determines the rate at which turbulent kinetic energy is
395 converted into thermal energy, directly influencing the vertical fluxes of momentum, heat, and mass.
396 Long-term measurements of TKEDR will enhance our understanding of boundary layer dynamic
397 processes and lead to more accurate simulations in atmospheric models.

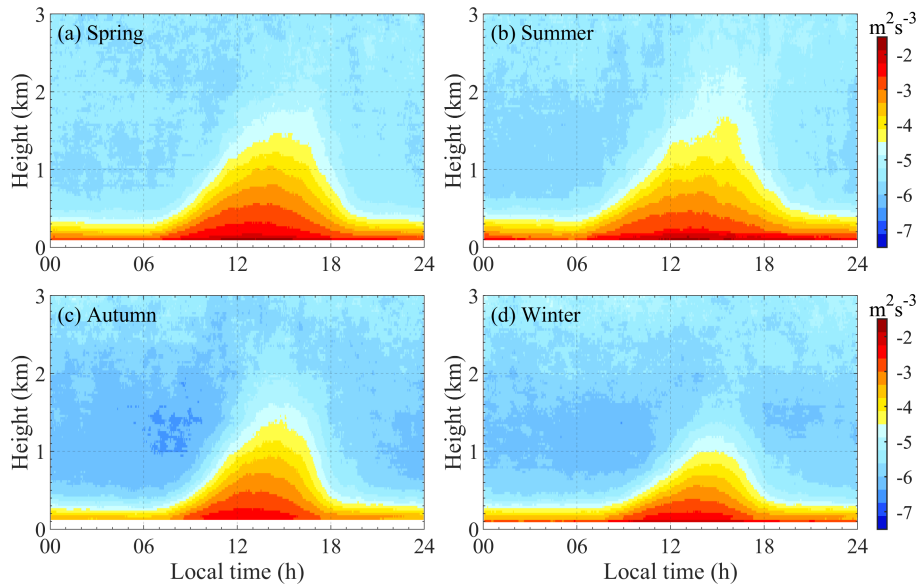


Figure 7. The same as Fig. 3 but for TKEDR.

398

399

400 Figure 7 illustrates the typical diurnal and seasonal cycles of the TKEDR profile. The TKEDR is
 401 highest near the surface, with typical values ranging from approximately 10^{-3} to $10^{-2} \text{ m}^2 \text{ s}^{-3}$, depending on
 402 the time of day and season. It decreases with height due to the diminishing influence of surface friction
 403 and thermal stratification. The convective boundary layer (or mixing layer) is clearly visible by noting
 404 where TKEDR is high. Diurnal variation starts from sunrise, as the increased temperature gradient
 405 between the surface and the above air enhances thermal buoyancy, which in turn promotes vertical
 406 convective mixing and turbulence. This causes TKEDR near the surface to grow and extend toward
 407 higher altitudes. In spring and summer, stronger and longer solar radiation leads to a more developed
 408 convective boundary layer, both in terms of duration and height, compared to autumn and winter. The
 409 convective boundary layer reaches its peak in the early afternoon, then begins to decay after 16:00 p.m.,
 410 eventually returning to a shallow well-mixed layer near the ground, approximately 350 m in spring and
 411 summer, and around 250 m in autumn and winter. During the night, a stable atmospheric layer was
 412 formed near the surface and turbulence was primarily driven by mechanical factors (e.g., wind shear)
 413 rather than thermal convection. The complex urban surface roughness enhances wind friction, resulting
 414 in intensified turbulence, particularly during spring and summer when nocturnal LLJs occur more
 415 frequently. This increased turbulence contributes to the elevated TKEDR observed at night during these
 416 seasons.

417 As TKEDR decreases with altitude, its contour lines (though not explicitly plotted but evident from
 418 the color gradations in Figure 7) display a right-skewed shape, with a delayed peak time. This delay can
 419 be attributed to two factors: first, convective mixing activity takes time to propagate upward from the
 420 surface. Second, the ground cools more rapidly than the air in the late afternoon. Consequently,
 421 turbulence at higher altitudes lags low-level activity, reflecting the thermal-driven development of
 422 turbulence and energy within the atmospheric boundary layer.

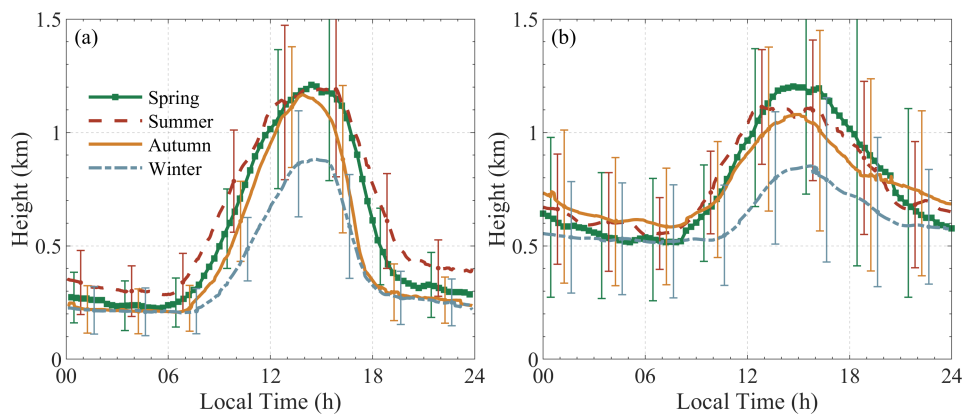
423 Here, we define the top of the convective boundary layer as the height where TKEDR reaches 10^{-4}
 424 $\text{ m}^2 \text{ s}^{-3}$. It should be noted that this height can be different from the MLH given in the next section (Sect.
 425 3.6), where the seasonal average MLH is calculated from the daily MLHs. We can see that the top of the
 426 convective boundary layer during daytime in summer exhibits dramatic fluctuations, as shown in Figure
 427 7(b), which could be attributed to the deep convective activities in the afternoon. Unstable atmospheric

428 stratification enhances vertical convection, leading to the formation of local convective clouds and
429 thunderstorms. These clouds reduce the amount of solar radiation reaching the surface, causing localized
430 cooling. Additionally, this process exacerbates the unevenness in the horizontal distribution of
431 temperature in the affected areas.

432 Overall, these seasonal and diurnal variations in TKEDR highlight the complex interactions
433 between surface properties, atmospheric stability, and weather systems in shaping the turbulence
434 characteristics within the boundary layer.

435 3.6 Seasonal variation of diurnal MLH for clear and cloudy days

436 The diurnal variations of MLH and BLH across different seasons in Hefei are depicted in Figure
437 8(a) and (b), respectively. The MLH is based on turbulence activities, while the BLH is based on the
438 vertical distribution of material (here aerosol). Therefore, both reflect the diurnal cycle of atmospheric
439 boundary layer dynamics, but there are some differences.



440

441 **Figure 8.** Time series of seasonal average (a) MLH and (b) BLH at Hefei. The error bars represent one standard
442 deviation $\pm\sigma$, and their positions (corresponding to time) vary slightly in different seasons to facilitate comparison.

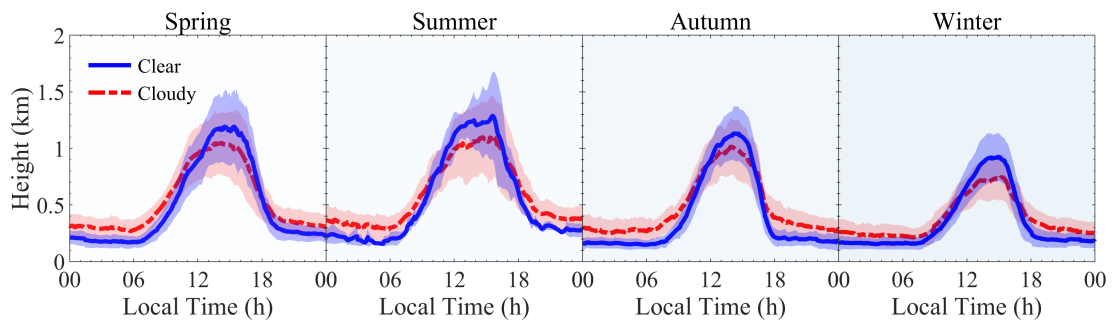
443 After sunrise, surface heating induced by solar radiation promotes the development of vertical
444 convective mixing and drives the surface aerosols upward. When the temperature gradient between the
445 surface and air reaches its maximum, the MLH rises fastest, which appears at about 9:00-10:00 a.m. This
446 time varies with seasons, just as the sunrise time, with the earliest in summer, followed by spring, autumn,
447 and winter. The value of MLH at a certain time also shows the same seasonal relationship, except for the
448 afternoon in summer. Although solar radiation is highest at noon, the short-wave incident radiation
449 received by the surface in the afternoon is still greater than the long-wave outgoing radiation. Therefore,
450 the MLH continues to grow, reaching its maximum between 2:00 p.m. and 3:00 p.m. with about 1.2 km
451 in spring and summer, slightly lower in autumn, and 0.8 km in winter.

452 The similar afternoon peak of MLH between summer and spring could be attributed to several
453 factors. In the northern hemisphere, the summer solstice which occurs around June 21st or 22nd, is
454 relatively close to the spring period. This timing means that the transition from spring to summer is not
455 always abrupt. Furthermore, high surface temperatures and increased evapotranspiration during summer
456 lead to frequent convective clouds and precipitation. These factors reduce solar radiation received by the
457 ground and weaken convective mixing, which can suppress the MLH. As a result, the seasonally average
458 MLH reflects these cloudy conditions, leading to a peak height that may not be as high as one might
459 expect on clear days.

460 In the late afternoon, as surface temperatures decrease due to radiative cooling, vertical convection

461 weakens and turbulence kinetic energy dissipates more rapidly, leading to a faster decline in MLH
 462 compared to its increase in the morning. Meanwhile, the decrease in BLH is more gradual due to the
 463 slower rate of dry deposition of aerosols. It is noteworthy that the BLH curves exhibit larger fluctuations
 464 and significantly higher standard deviations compared to the MLH curves. This is primarily due to the
 465 considerable retrieval uncertainty in BLH measurements, which are influenced by aerosol distribution.
 466 Transboundary aerosols, clouds, and multilayer aerosols (e.g., residual layer) frequently affect these
 467 measurements, a well-recognized issue with aerosol-based BLH retrieval methods (Dang et al., 2019;
 468 Mei et al., 2022; Kotthaus et al., 2023; Barlow et al., 2011).

469 During the night, the temperature inversion layer inhibits vertical thermal convection and mixing.
 470 Instead, mechanical mixing driven by wind shear becomes predominant, especially in the presence of
 471 low-level jets. Consequently, the MLH is typically highest in summer at about 0.3 km, followed by spring,
 472 and lowest in autumn and winter, about 0.2 km. In contrast, The BLH remains higher than the MLH, at
 473 approximately 0.5~0.7 km. The higher nocturnal BLH in autumn may be related to the transboundary
 474 transport of aerosols and meteorological factors. Both the MLH and the BLH continue to decrease and
 475 reach their minimum at sunrise in the next diurnal cycle.



476

477 **Figure 9.** Time series of seasonal average MLH (lines) and one-sigma standard deviation (shaded areas) for clear
 478 days and cloudy days at Hefei.

479 To further investigate the influence of clouds on the development of MLH, we compared the
 480 seasonally averaged diurnal MLH under different weather conditions, as shown in Figure 9. The diurnal
 481 MLH showed significant differences between clear and cloudy days and exhibited similar characteristics
 482 in each season. Overall, the diurnal variation of MLH was less pronounced on cloudy days with a flatter
 483 curve, due to the modulation of clouds on the surface radiation budget. During daytime, the presence of
 484 clouds typically reduces surface heating by solar radiation, which inhibits the development of vertical
 485 convective mixing and results in a shallower mixed layer compared to clear weather conditions. The
 486 difference of MLH reaches its maximum of about 200 m in the afternoon. While during the night, clouds
 487 act as a "greenhouse" by absorbing longwave radiation from the ground and slowing down the radiative
 488 cooling, which results in a higher MLH compared to clear days. The mean difference in MLH between
 489 cloudy and clear days is about 100 m.

490 Note that, the diurnal MLH in summer showed relatively large variations, particularly on clear days.
 491 This variability can be attributed to strong and variable convective activity, as well as to the limited
 492 number of data samples. Plum rains and frequent convective clouds in summer lead to a much lower
 493 proportion of sunny days than in other seasons.

494 **4. Conclusions and discussion**

495 This study utilized three years of Doppler wind lidar measurements (from June 2019 to June 2022)

496 to characterize the PBL dynamics over Hefei, a rapidly developing city in the western YRD, China. By
497 analyzing key parameters such as wind profiles, low-level jets, turbulence, and boundary layer height,
498 this study provides a detailed characterization of the seasonal and diurnal variability of urban PBL
499 dynamics in a monsoon-influenced subtropical environment.

500 The results showed that HWS steady increase from 2 to 7 m s⁻¹ between 300 m and 3 km AGL, with
501 a more rapid acceleration above 3 km, particularly in autumn and winter. Westerly winds (270°±15°)
502 dominated above 3 km, while wind directions within the PBL were more variable, influenced by local
503 topography and surface roughness. LLJs primarily formed at sunset and dissipated by noon, typically
504 occurring at altitudes between 0.5 and 0.6 km throughout the year, except in July. LLJ occurrences were
505 most frequent in spring (31.7%), followed by summer (24.7%), autumn (22.3%), and winter (21.3%),
506 with the strongest LLJs observed in summer, extending up to 1.5 km.

507 Strong wind speed gradients below the LLJs induced large VWSH (up to 0.02 s⁻¹) and elevated
508 TKEDR (up to 10⁻² m²s⁻³) in the near-surface layer at night, promoting vertical mixing of pollutants.
509 Seasonal wind direction shifts of LLJ nose (e.g., southerly in summer and northeasterly in winter)
510 reflected the interplay between monsoonal flows and local topography. During the daytime, TKEDR
511 increased and extend toward higher altitudes with the transport of heat, momentum and mass. Turbulence
512 mixing slowed down wind speeds by increasing surface friction, forming a gentler wind zone and
513 reducing shear intensity. An interesting fluctuation in TKEDR above the MLH top during early summer
514 afternoons was attributed to atmospheric instability after continuous surface heating.

515 The dynamics-based MLH exhibited smaller fluctuations and lower standard deviations compared
516 to the aerosol-based BLH. The MLH peaked between 2:00 p.m. and 3:00 p.m., reaching ~1.2 km in
517 spring and summer, slightly lower in autumn, and around 0.8 km in winter. After sunset, it eventually
518 returned to a shallow well-mixed layer near the ground (~350 m in spring and summer, and ~250 m in
519 autumn and winter). Compared to clear days, cloud cover reduces the MLH by about 200 m at the
520 afternoon peak time, while increasing it by approximately 100 m at night. These results quantified the
521 different influence of cloud coverage to the development of MLH during day and night.

522 In conclusion, this study leverages the high temporal and spatial resolution of Doppler wind lidar to
523 provide a detailed characterization of urban PBL dynamics, offering valuable insights into their complex
524 interactions with surface heating and cooling, atmospheric stability, cloud, and synoptic-scale weather
525 systems. Long-term lidar observations of LLJs, MLH, and TKEDR provide critical insights into vertical
526 mixing, turbulence, and pollutant transport in a monsoon-influenced subtropical environment, enriching
527 the climatological understanding of LLJs and PBL processes over the western Yangtze River Delta. These
528 results have also significant practical implications, serving as valuable references for local standards and
529 regional planning by supporting strategies for urban air quality management and the development of low-
530 altitude economic activities. Specifically, the results inform vertical zoning for applications such as wind
531 energy development and drone logistics, guiding optimal turbine placement and flight route planning.
532 Overall, this study underscores the importance of lidar-based observations in addressing regional
533 atmospheric challenges and advancing environmental and economic sustainability.

534 Despite these insights, this study is constrained to a single urban observational site and focuses on
535 statistical analysis. Future research will extend observations to multiple sites, including urban, suburban,
536 and rural to comprehensively capture the spatial variability of PBL processes and LLJ characteristics
537 across different land-use types and topographic conditions. Additionally, subsequent studies will conduct
538 specific case analyses under varying meteorological scenarios, integrating aerosol observations and high-
539 resolution numerical models. These efforts aim to enhance our understanding of the interactions between

540 aerosols, clouds, radiation, and PBL dynamics, particularly their influence on vertical mixing and
541 boundary layer evolution.

542

543 **Data Availability.** The Doppler wind lidar data used in this study can be provided for non-commercial
544 research purposes upon request to the first author (Tianwen Wei: twwei@nuist.edu.cn).

545

546 **Author contributions.** Tianwen Wei: Conceptualization, Methodology, Data curation, Formal analysis,
547 Visualization, Writing – review & editing. Mengya Wang: Conceptualization, Writing – original draft,
548 Methodology, Investigation. Kenan Wu: Resources, Data curation. Jinlong Yuan: Resources, Data
549 curation. Haiyun Xia: Conceptualization, Supervision, Resources, Validation. Simone Lolli: Writing –
550 review & editing, Validation.

551

552 **Conflict of Interest.** Some authors are members of the editorial board of Atmospheric Measurement
553 Techniques.

554

555 **Financial support.** This work was supported by the National Natural Science Foundation of China
556 (42405136), the China Meteorological Administration Xiong'an Atmospheric Boundary Layer Key
557 Laboratory (2023LABL-B11), the Natural Science Research of Jiangsu Higher Education Institutions of
558 China (23KJB170012).

559

560 Reference

- 561 Baklanov, A. A., Grisogono, B., Bornstein, R., Mahrt, L., Zilitinkevich, S. S., Taylor, P., Larsen, S. E., Rotach, M. W., and Fernando,
562 H. J. S.: The nature, theory, and modeling of atmospheric planetary boundary layers, *Bull. Am. Meteorol. Soc.*, 92, 123–128,
563 <https://doi.org/10.1175/2010BAMS2797.1>, 2011.
- 564 Banakh, V. A., Brewer, A., Pichugina, E. L., and Smalikho, I. N.: Measurements of wind velocity and direction with coherent
565 doppler lidar in conditions of a weak echo signal, *Atmospheric Ocean. Opt.*, 23, 381–388,
566 <https://doi.org/10.1134/S1024856010050076>, 2010.
- 567 Banakh, V. A., Smalikho, I. N., and Falits, A. V.: Estimation of the turbulence energy dissipation rate in the atmospheric boundary
568 layer from measurements of the radial wind velocity by micropulse coherent doppler lidar, *Opt. Express*, 25, 22679,
569 <https://doi.org/10.1364/oe.25.022679>, 2017.
- 570 Banakh, V. A., Smalikho, I. N., and Falits, A. V.: Estimation of the height of the turbulent mixing layer from data of doppler lidar
571 measurements using conical scanning by a probe beam, *Atmospheric Meas. Tech.*, 14, 1511–1524,
572 <https://doi.org/10.5194/amt-14-1511-2021>, 2021.
- 573 Barlow, J. F.: Progress in observing and modelling the urban boundary layer, *Urban Clim.*, 10, 216–240,
574 <https://doi.org/10.1016/j.uclim.2014.03.011>, 2014.
- 575 Barlow, J. F., Dunbar, T. M., Nemitz, E. G., Wood, C. R., Gallagher, M. W., Davies, F., O'Connor, E., and Harrison, R. M.: Boundary
576 layer dynamics over London, UK, as observed using Doppler lidar during REPARTEE-II, *Atmospheric Chem. Phys.*, 11,
577 2111–2125, <https://doi.org/10.5194/acp-11-2111-2011>, 2011.
- 578 Blackadar, A. K.: Boundary layer wind maxima and their significance for the growth of nocturnal inversions, *Bull. Am. Meteorol.*
579 *Soc.*, 38, 283–290, <https://doi.org/10.1175/1520-0477-38.5.283>, 1957.
- 580 Caicedo, V., Rappenglück, B., Lefter, B., Morris, G., Toledo, D., and Delgado, R.: Comparison of aerosol lidar retrieval methods
581 for boundary layer height detection using ceilometer aerosol backscatter data, *Atmospheric Meas. Tech.*, 10, 1609–1622,
582 <https://doi.org/10.5194/amt-10-1609-2017>, 2017.
- 583 Caughey, S. J. and Palmer, S. G.: Some aspects of turbulence structure through the depth of the convective boundary layer, *Q. J.*
584 *R. Meteorol. Soc.*, 105, 811–827, <https://doi.org/10.1002/qj.49710544606>, 1979.
- 585 Chen, S., Tong, B., Russell, L. M., Wei, J., Guo, J., Mao, F., Liu, D., Huang, Z., Xie, Y., Qi, B., Zhang, H., Sun, Y., Zhang, B., Xu,

586 C., Wu, L., and Liu, D.: Lidar-based daytime boundary layer height variation and impact on the regional satellite-based PM2.5
587 estimate, *Remote Sens. Environ.*, 281, 113224, <https://doi.org/10.1016/j.rse.2022.113224>, 2022.

588 Chen, Y., Zhang, A., Zhang, Y., Cui, C., Wan, R., Wang, B., and Fu, Y.: A heavy precipitation event in the Yangtze River basin led
589 by an eastward moving tibetan plateau cloud system in the summer of 2016, *J. Geophys. Res. Atmospheres*, 125,
590 e2020JD032429, <https://doi.org/10.1029/2020JD032429>, 2020.

591 Chen, Y.-C., Xue, L., Lebo, Z. J., Wang, H., Rasmussen, R. M., and Seinfeld, J. H.: A comprehensive numerical study of aerosol-
592 cloud-precipitation interactions in marine stratocumulus, *Atmospheric Chem. Phys.*, 11, 9749–9769,
593 <https://doi.org/10.5194/acp-11-9749-2011>, 2011.

594 Christensen, M. W., Wu, P., Varble, A. C., Xiao, H., and Fast, J. D.: Aerosol-induced closure of marine cloud cells: enhanced effects
595 in the presence of precipitation, *Atmospheric Chem. Phys.*, 24, 6455–6476, <https://doi.org/10.5194/acp-24-6455-2024>, 2024.

596 Cui, C., Zhou, W., Yang, H., Wang, X., Deng, Y., Wang, X., Xu, G., and Wang, J.: Analysis of the characteristics of the low-level
597 jets in the middle reaches of the Yangtze River during the mei-yu season, *Adv. Atmospheric Sci.*, 40, 711–724,
598 <https://doi.org/10.1007/s00376-022-2107-1>, 2023.

599 Dang, R., Yang, Y., Li, H., Hu, X.-M., Wang, Z., Huang, Z., Zhou, T., and Zhang, T.: Atmosphere boundary layer height (ABLH)
600 determination under multiple-layer conditions using micro-pulse lidar, *Remote Sens.*, 11, 263,
601 <https://doi.org/10.3390/rs11030263>, 2019.

602 Du, Y., Zhang, Q., Chen, Y., Zhao, Y., and Wang, X.: Numerical simulations of spatial distributions and diurnal variations of low-
603 level jets in China during early summer, *J. Clim.*, 27, 5747–5767, <https://doi.org/10.1175/JCLI-D-13-00571.1>, 2014.

604 Fochesatto, G. J., Drobinski, P., Flamant, C., Guedalia, D., Sarrat, C., Flamant, P. H., and Pelon, J.: Evidence of dynamical coupling
605 between the residual layer and the developing convective boundary layer, *Bound.-Layer Meteorol.*, 99, 451–464,
606 <https://doi.org/10.1023/A:1018935129006>, 2001.

607 Garratt, J.: Review: the atmospheric boundary layer, *Earth-Sci. Rev.*, 37, 89–134, [https://doi.org/10.1016/0012-8252\(94\)90026-4](https://doi.org/10.1016/0012-8252(94)90026-4),
608 1994.

609 Gu, L., Yao, J., Hu, Z., Ma, Y., Sun, F., Yu, H., Wang, S., Yang, Y., Guo, R., and Qin, Y.: Characteristics of the atmospheric boundary
610 layer's structure and heating (cooling) rate in summer over the northern Tibetan Plateau, *Atmospheric Res.*, 269, 106045,
611 <https://doi.org/10.1016/j.atmosres.2022.106045>, 2022.

612 Guo, J., Li, Y., Cohen, J. B., Li, J., Chen, D., Xu, H., Liu, L., Yin, J., Hu, K., and Zhai, P.: Shift in the temporal trend of boundary
613 layer height in China using long-term (1979–2016) radiosonde data, *Geophys. Res. Lett.*, 46, 6080–6089,
614 <https://doi.org/10.1029/2019GL082666>, 2019.

615 Guo, J., Zhang, J., Yang, K., Liao, H., Zhang, S., Huang, K., Lv, Y., Shao, J., Yu, T., Tong, B., Li, J., Su, T., Yim, S. H. L., Stoffelen,
616 A., Zhai, P., and Xu, X.: Investigation of near-global daytime boundary layer height using high-resolution radiosondes: first
617 results and comparison with ERA5, MERRA-2, JRA-55, and NCEP-2 reanalyses, *Atmospheric Chem. Phys.*, 21, 17079–
618 17097, <https://doi.org/10.5194/acp-21-17079-2021>, 2021.

619 Hu, F., Xie, P., Xu, J., Li, A., Lv, Y., Zhang, Z., Zheng, J., and Tian, X.: Impacts of synoptic weather patterns on hefei's ozone in
620 warm season and analysis of transport pathways during extreme pollution events, *J. Environ. Sci.*,
621 <https://doi.org/10.1016/j.jes.2024.06.032>, 2024.

622 Huang, M., Gao, Z., Miao, S., Chen, F., LeMone, M. A., Li, J., Hu, F., and Wang, L.: Estimate of boundary-layer depth over beijing,
623 china, using doppler lidar data during SURF-2015, *Bound.-Layer Meteorol.*, 162, 503–522, <https://doi.org/10.1007/s10546-016-0205-2>, 2017.

624 Jia, M., Yuan, J., Wang, C., Xia, H., Wu, Y., Zhao, L., Wei, T., Wu, J., Wang, L., Gu, S. Y., Liu, L., Lu, D., Chen, R., Xue, X., and
625 Dou, X.: Long-lived high-frequency gravity waves in the atmospheric boundary layer: Observations and simulations,
626 *Atmospheric Chem. Phys.*, 19, 15431–15446, <https://doi.org/10.5194/acp-19-15431-2019>, 2019.

627 Jiang, P., Yuan, J., Wu, K., Wang, L., and Xia, H.: Turbulence detection in the atmospheric boundary layer using coherent doppler
628 wind lidar and microwave radiometer, *Remote Sens.*, 14, 2951, <https://doi.org/10.3390/rs14122951>, 2022.

629 Justus, C. G., Hargraves, W. R., Mikhail, A., and Graber, D.: Methods for estimating wind speed frequency distributions, *J. Appl.*
630 *Meteorol.*, 17, 350–353, [https://doi.org/10.1175/1520-0450\(1978\)017<0350:MFEWSF>2.0.CO;2](https://doi.org/10.1175/1520-0450(1978)017<0350:MFEWSF>2.0.CO;2), 1978.

631 Kang, H., Zhu, B., Gao, J., He, Y., Wang, H., Su, J., Pan, C., Zhu, T., and Yu, B.: Potential impacts of cold frontal passage on air
632 quality over the Yangtze River delta, china, *Atmospheric Chem. Phys.*, 19, 3673–3685, [https://doi.org/10.5194/acp-19-3673-](https://doi.org/10.5194/acp-19-3673-2019)
633 2019, 2019.

634 Kim, C. P. and Entekhabi, D.: Feedbacks in the land-surface and mixed-layer energy budgets, *Bound.-Layer Meteorol.*, 88, 1–21,
635 <https://doi.org/10.1023/A:1001094008513>, 1998.

636 Kotthaus, S., Bravo-Aranda, J. A., Collaud Coen, M., Guerrero-Rascado, J. L., Costa, M. J., Cimini, D., O'Connor, E. J., Hervo,
637 M., Alados-Arboledas, L., Jiménez-Portaz, M., Mona, L., Ruffieux, D., Illingworth, A., and Haefelin, M.: Atmospheric
638 boundary layer height from ground-based remote sensing: a review of capabilities and limitations, *Atmospheric Meas. Tech.*,
639 16, 433–479, <https://doi.org/10.5194/amt-16-433-2023>, 2023.

640 Li, C., Li, H., Zhang, Y., Zha, D., Zhao, B., Yang, S., Zhang, B., and De Boer, W. F.: Predicting hydrological impacts of the Yangtze-
641 to-huaihe water diversion project on habitat availability for wintering waterbirds at caizi lake, *J. Environ. Manage.*, 249,
642 109251, <https://doi.org/10.1016/j.jenvman.2019.07.022>, 2019.

643

644 Li, L., Zhu, A., Huang, L., Wang, Q., Chen, Y., Ooi, M. C. G., Wang, M., Wang, Y., and Chan, A.: Modeling the impacts of land
645 use/land cover change on meteorology and air quality during 2000–2018 in the Yangtze River delta region, china, *Sci. Total*
646 *Environ.*, 829, 154669, <https://doi.org/10.1016/j.scitotenv.2022.154669>, 2022a.

647 Li, L., Wang, Y., Lu, J., Wang, X., Wu, P., and Tao, Y.: Spatial and temporal variability of maximum wind speed and extreme wind
648 speed in Anhui Province during different recurrence intervals from 1981 to 2020, *J. Trop. Meteorol.*, 38, 662–670,
649 <https://doi.org/10.16032/j.issn.1004-4965.2022.060>, 2022b.

650 Li, X., Li, Q.-P., Ding, Y.-H., and Wang, M.: Near-surface wind speed changes in eastern China during 1970–2019 winter and its
651 possible causes, *Adv. Clim. Change Res.*, 13, 228–239, <https://doi.org/10.1016/j.accre.2022.01.003>, 2022c.

652 Li, X.-B., Han, Y.-X., Fu, Z.-Y., Zhang, Y.-C., Fan, M., Sang, S.-J., Chen, X.-X., Liang, B.-Y., Liu, Y.-C., Lu, P.-C., Li, H.-W., Pan,
653 H.-F., and Yang, J.-M.: Association of sudden sensorineural hearing loss with meteorological factors: a time series study in
654 hefei, china, and a literature review, *Environ. Sci. Pollut. Res.*, 31, 42970–42990, [https://doi.org/10.1007/s11356-024-33943-](https://doi.org/10.1007/s11356-024-33943-1)
655 [1](https://doi.org/10.1007/s11356-024-33943-1), 2024.

656 Li, Z., Guo, J., Ding, A., Liao, H., Liu, J., Sun, Y., Wang, T., Xue, H., Zhang, H., and Zhu, B.: Aerosol and boundary-layer
657 interactions and impact on air quality, *Natl. Sci. Rev.*, 4, 810–833, <https://doi.org/10.1093/nsr/nwx117>, 2017.

658 Li, Z., Song, L., Ma, H., Xiao, J., Wang, K., and Chen, L.: Observed surface wind speed declining induced by urbanization in east
659 China, *Clim. Dyn.*, 50, 735–749, <https://doi.org/10.1007/s00382-017-3637-6>, 2018.

660 Liu, H., Huang, X., Fei, J., Zhang, C., and Cheng, X.: Spatiotemporal features and associated synoptic patterns of extremely
661 persistent heavy rainfall over china, *J. Geophys. Res. Atmospheres*, 127, e2022JD036604,
662 <https://doi.org/10.1029/2022JD036604>, 2022.

663 Liu, L., Liang, Y., He, C., Li, B., Chu, L., and Li, J.: Evaluating the contribution of climate change and urbanization to the reversal
664 in maximum surface wind speed decline: case study in the Yangtze River economic belt, china, *Urban Clim.*, 52, 101713,
665 <https://doi.org/10.1016/j.uclim.2023.101713>, 2023.

666 Liu, X., Guo, Q., Guo, Z., Yin, Z.-Y., Dong, B., and Smith, R.: Where were the monsoon regions and arid zones in Asia prior to
667 the Tibetan Plateau uplift?, *Natl. Sci. Rev.*, 2, 403–416, <https://doi.org/10.1093/nsr/nwv068>, 2015.

668 Madala, S., Satyanarayana, A. N. V., and Rao, T. N.: Performance evaluation of PBL and cumulus parameterization schemes of
669 WRF ARW model in simulating severe thunderstorm events over gadanki MST radar facility — case study, *Atmospheric Res.*,
670 139, 1–17, <https://doi.org/10.1016/j.atmosres.2013.12.017>, 2014.

671 Manninen, A. J., Marke, T., Tuononen, M., and O’Connor, E. J.: Atmospheric boundary layer classification with doppler lidar, *J.*
672 *Geophys. Res. Atmospheres*, 123, 8172–8189, <https://doi.org/10.1029/2017JD028169>, 2018.

673 Mei, L., Wang, X., Gong, Z., Liu, K., Hua, D., and Wang, X.: Retrieval of the planetary boundary layer height from lidar
674 measurements by a deep-learning method based on the wavelet covariance transform, *Opt. Express*, 30, 16297,
675 <https://doi.org/10.1364/OE.454094>, 2022.

676 Miao, Y., Guo, J., Liu, S., Wei, W., Zhang, G., Lin, Y., and Zhai, P.: The climatology of low-level jet in beijing and guangzhou,
677 china, *J. Geophys. Res. Atmospheres*, 123, 2816–2830, <https://doi.org/10.1002/2017JD027321>, 2018.

678 Mirza, A. K., Dacre, H. F., and Lo, C. H. B.: A case study analysis of the impact of a new free tropospheric turbulence scheme on
679 the dispersion of an atmospheric tracer, *Q. J. R. Meteorol. Soc.*, 150, 1907–1925, <https://doi.org/10.1002/qj.4681>, 2024.

680 O’Connor, E. J., Illingworth, A. J., Brooks, I. M., Westbrook, C. D., Hogan, R. J., Davies, F., and Brooks, B. J.: A method for
681 estimating the turbulent kinetic energy dissipation rate from a vertically pointing doppler lidar, and independent evaluation
682 from balloon-borne in situ measurements, *J. Atmospheric Ocean. Technol.*, 27, 1652–1664,
683 <https://doi.org/10.1175/2010jtecha1455.1>, 2010.

684 Ortiz-Amezcu, P., Andújar-Maqueda, J., Manninen, A. J., Pentikäinen, P., O’Connor, E. J., Stachlewska, I. S., De Arruda Moreira,
685 G., Benavent-Oltra, J. A., Casquero-Vera, J. A., Poczta, P., Wang, D., Harenda, K. M., Chojnicki, B. H., Szczepanik, D. M.,
686 Janicka, L., Schüttemeyer, D., Alados-Arboledas, L., and Guerrero-Rascado, J. L.: Dynamics of the atmospheric boundary
687 layer over two middle-latitude rural sites with doppler lidar, *Atmospheric Res.*, 280, 106434,
688 <https://doi.org/10.1016/j.atmosres.2022.106434>, 2022.

689 Parsons, D. B.: An explanation for intense frontal updrafts and narrow cold-frontal rainbands, *J. Atmospheric Sci.*, 49, 1810–1825,
690 [https://doi.org/10.1175/1520-0469\(1992\)049<1810:AEFIFU>2.0.CO;2](https://doi.org/10.1175/1520-0469(1992)049<1810:AEFIFU>2.0.CO;2), 1992.

691 Pérez-Ramírez, D., Whiteman, D. N., Veselovskii, I., Colarco, P., Korenski, M., and da Silva, A.: Retrievals of aerosol single
692 scattering albedo by multiwavelength lidar measurements: Evaluations with NASA langley HSRL-2 during discover-AQ field
693 campaigns, *Remote Sens. Environ.*, 222, 144–164, <https://doi.org/10.1016/j.rse.2018.12.022>, 2019.

694 Pérez-Ramírez, D., Whiteman, D. N., Veselovskii, I., Ferrare, R., Titos, G., Granados-Muñoz, M. J., Sánchez-Hernández, G., and
695 Navas-Guzmán, F.: Spatiotemporal changes in aerosol properties by hygroscopic growth and impacts on radiative forcing and
696 heating rates during DISCOVER-AQ 2011, *Atmospheric Chem. Phys.*, 21, 12021–12048, [https://doi.org/10.5194/acp-21-](https://doi.org/10.5194/acp-21-12021-2021)
697 [12021-2021](https://doi.org/10.5194/acp-21-12021-2021), 2021.

698 Petrosyan, A., Galperin, B., Larsen, S. E., Lewis, S. R., Määttänen, A., Read, P. L., Renno, N., Rogberg, L. P. H. T., Savijärvi, H.,
699 Siili, T., Spiga, A., Toigo, A., and Vázquez, L.: The martian atmospheric boundary layer, *Rev. Geophys.*, 49, 2010RG000351,
700 <https://doi.org/10.1029/2010RG000351>, 2011.

701 Pobočíková, I., Sedláčková, Z., and Michalková, M.: Application of four probability distributions for wind speed modeling,

702 Procedia Eng., 192, 713–718, <https://doi.org/10.1016/j.proeng.2017.06.123>, 2017.

703 Qin, R. X., Xiao, C., Zhu, Y., Li, J., Yang, J., Gu, S., Xia, J., Su, B., Liu, Q., and Woodward, A.: The interactive effects between

704 high temperature and air pollution on mortality: a time-series analysis in hefei, china, *Sci. Total Environ.*, 575, 1530–1537,

705 <https://doi.org/10.1016/j.scitotenv.2016.10.033>, 2017.

706 Qiu, Z., Xian, J., Yang, Y., Lu, C., Yang, H., Hu, Y., Sun, J., and Zhang, C.: Characteristics of coastal low-level jets in the boundary

707 layer of the pearl river estuary, *J. Mar. Sci. Eng.*, 11, 1128, <https://doi.org/10.3390/jmse11061128>, 2023.

708 Rife, D. L., Pinto, J. O., Monaghan, A. J., Davis, C. A., and Hannan, J. R.: Global distribution and characteristics of diurnally

709 varying low-level jets, *J. Clim.*, 23, 5041–5064, <https://doi.org/10.1175/2010jcli3514.1>, 2010.

710 Shen, L., Cheng, Y., Bai, X., Dai, H., Wei, X., Sun, L., Yang, Y., Zhang, J., Feng, Y., Li, Y. J., Chen, D.-R., Liu, J., and Gui, H.:

711 Vertical profile of aerosol number size distribution during a haze pollution episode in hefei, china, *Sci. Total Environ.*, 814,

712 152693, <https://doi.org/10.1016/j.scitotenv.2021.152693>, 2022.

713 Shi, C., Roth, M., Zhang, H., and Li, Z.: Impacts of urbanization on long-term fog variation in anhui province, china, *Atmos.*

714 *Environ.*, 42, 8484–8492, <https://doi.org/10.1016/j.atmosenv.2008.08.002>, 2008.

715 Sisterson, D. L. and Frenzen, P.: Nocturnal boundary-layer wind maxima and the problem of wind power assessment., *Environ.*

716 *Sci. Technol.*, 12, 218–221, <https://doi.org/10.1021/es60138a014>, 1978.

717 Smalikho, I.: Techniques of wind vector estimation from data measured with a scanning coherent doppler lidar, *J. Atmospheric*

718 *Ocean. Technol.*, 20, 276–291, [https://doi.org/10.1175/1520-0426\(2003\)020<0276:TOWVEF>2.0.CO;2](https://doi.org/10.1175/1520-0426(2003)020<0276:TOWVEF>2.0.CO;2), 2003.

719 Stull, R. B.: An introduction to boundary layer meteorology, Springer Science & Business Media, 688 pp., 1988.

720 Su, L., Lu, C., Yuan, J., Wang, X., He, Q., and Xia, H.: Measurement report: the promotion of low-level jet and thermal-effect on

721 development of deep convective boundary layer at the southern edge of the taklimakan desert,

722 <https://doi.org/10.5194/egusphere-2024-1010>, 15 May 2024.

723 Su, T., Li, Z., and Kahn, R.: Relationships between the planetary boundary layer height and surface pollutants derived from lidar

724 observations over china: regional pattern and influencing factors, *Atmospheric Chem. Phys.*, 18, 15921–15935,

725 <https://doi.org/10.5194/acp-18-15921-2018>, 2018.

726 Su, T., Li, Z., and Kahn, R.: A new method to retrieve the diurnal variability of planetary boundary layer height from lidar under

727 different thermodynamic stability conditions, *Remote Sens. Environ.*, 237, 111519, <https://doi.org/10.1016/j.rse.2019.111519>,

728 2020.

729 Sun, J. and Ongsomwang, S.: Impact of multitemporal land use and land cover change on land surface temperature due to

730 urbanization in hefei city, china, *ISPRS Int. J. Geo-Inf.*, 10, 809, <https://doi.org/10.3390/ijgi10120809>, 2021.

731 Sun, Y., Yin, H., Liu, C., Mahieu, E., Notholt, J., Té, Y., Lu, X., Palm, M., Wang, W., Shan, C., Hu, Q., Qin, M., Tian, Y., and Zheng,

732 B.: The reduction in C2H6 from 2015 to 2020 over hefei, eastern China, points to air quality improvement in China,

733 *Atmospheric Chem. Phys.*, 21, 11759–11779, <https://doi.org/10.5194/acp-21-11759-2021>, 2021.

734 Tamarin-Brodsky, T. and Hadas, O.: The asymmetry of vertical velocity in current and future climate, *Geophys. Res. Lett.*, 46,

735 374–382, <https://doi.org/10.1029/2018GL080363>, 2019.

736 Tuononen, M., O'Connor, E. J., Sinclair, V. A., and Vakkari, V.: Low-level jets over utö, finland, based on doppler lidar observations,

737 *J. Appl. Meteorol. Climatol.*, 56, 2577–2594, <https://doi.org/10.1175/JAMC-D-16-0411.1>, 2017.

738 Vivone, G., D'Amico, G., Summa, D., Lolli, S., Amodeo, A., Bortoli, D., and Pappalardo, G.: Atmospheric boundary layer height

739 estimation from aerosol lidar: a new approach based on morphological image processing techniques, *Atmospheric Chem.*

740 *Phys.*, 21, 4249–4265, <https://doi.org/10.5194/acp-21-4249-2021>, 2021.

741 Wang, C., Zhou, J., Zhou, S., Zhang, Y., and Zhang, M.: Distribution characteristics of wind in anhui province during 1981 -2012,

742 *J. Arid Meteorol.*, 33, 236–243, [https://doi.org/10.11755/i.issn.1006-7639\(2015\)-02-0236](https://doi.org/10.11755/i.issn.1006-7639(2015)-02-0236), 2015a.

743 Wang, C., Jia, M., Xia, H., Wu, Y., Wei, T., Shang, X., Yang, C., Xue, X., and Dou, X.: Relationship analysis of PM2.5 and boundary

744 layer height using an aerosol and turbulence detection lidar, *Atmospheric Meas. Tech.*, 12, 3303–3315,

745 <https://doi.org/10.5194/amt-12-3303-2019>, 2019.

746 Wang, H., Li, Z., Lv, Y., Zhang, Y., Xu, H., Guo, J., and Goloub, P.: Determination and climatology of the diurnal cycle of the

747 atmospheric mixing layer height over beijing 2013–2018: lidar measurements and implications for air pollution, *Atmospheric*

748 *Chem. Phys.*, 20, 8839–8854, <https://doi.org/10.5194/acp-20-8839-2020>, 2020.

749 Wang, L., Qiang, W., Xia, H., Wei, T., Yuan, J., and Jiang, P.: Robust solution for boundary layer height detections with coherent

750 doppler wind lidar, *Adv. Atmospheric Sci.*, 38, 1920–1928, <https://doi.org/10.1007/s00376-021-1068-0>, 2021.

751 Wang, M., Fang, X., Hu, S., Hu, H., Li, T., and Dou, X.: Variation characteristics of water vapor distribution during 2000-2008

752 over hefei (31.9°N, 117.2°E) observed by L625 lidar, *Atmospheric Res.*, 164–165, 1–8,

753 <https://doi.org/10.1016/j.atmosres.2015.04.003>, 2015b.

754 Wang, M., Wei, T., Lolli, S., Wu, K., Wang, Y., Hu, H., Yuan, J., Tang, D., and Xia, H.: A long-term doppler wind LiDAR study of

755 heavy pollution episodes in western Yangtze River delta region, china, *Atmospheric Res.*, 310, 107616,

756 <https://doi.org/10.1016/j.atmosres.2024.107616>, 2024.

757 Wang, S., Wang, Q., Jordan, R. E., and Persson, P. O. G.: Interactions among longwave radiation of clouds, turbulence, and snow

758 surface temperature in the arctic: a model sensitivity study, *J. Geophys. Res. Atmospheres*, 106, 15323–15333,

759 <https://doi.org/10.1029/2000JD900358>, 2001.

760 Wang, Y., Hu, H., Ren, X., Yang, X.-Q., and Mao, K.: Significant northward jump of the western pacific subtropical high: The
761 interannual variability and mechanisms, *J. Geophys. Res. Atmospheres*, 128, e2022JD037742, <https://doi.org/10.1029/2022JD037742>, 2023.

762
763 Wei, T., Xia, H., Hu, J., Wang, C., Shangguan, M., Wang, L., Jia, M., and Dou, X.: Simultaneous wind and rainfall detection by
764 power spectrum analysis using a VAD scanning coherent doppler lidar, *Opt. Express*, 27, 31235–31245, <https://doi.org/10.1364/OE.27.031235>, 2019.

765
766 Wei, T., Xia, H., Wu, Y., Yuan, J., Wang, C., and Dou, X.: Inversion probability enhancement of all-fiber CDWL by noise modeling
767 and robust fitting, *Opt. Express*, 28, 29662, <https://doi.org/10.1364/oe.401054>, 2020.

768
769 Wei, T., Xia, H., Yue, B., Wu, Y., and Liu, Q.: Remote sensing of raindrop size distribution using the coherent doppler lidar, *Opt.
770 Express*, 29, 17246–17257, <https://doi.org/10.1364/OE.426326>, 2021.

771
772 Wei, T., Xia, H., Wu, K., Yang, Y., Liu, Q., and Ding, W.: Dark/bright band of a melting layer detected by coherent doppler lidar
773 and micro rain radar, *Opt. Express*, 30, 3654–3663, <https://doi.org/10.1364/OE.450714>, 2022.

774
775 Wei, T., Wang, M., Jiang, P., Wu, K., Zhang, Z., Yuan, J., Xia, H., and Lolli, S.: Retrieving aerosol backscatter coefficient using
776 coherent doppler wind lidar, *Opt. Express*, 33, 6832–6849, <https://doi.org/10.1364/OE.551730>, 2025.

777
778 Wei, W., Wu, B. G., Ye, X. X., Wang, H. X., and Zhang, H. S.: Characteristics and mechanisms of low-level jets in the Yangtze
779 River delta of China, *Bound.-Layer Meteorol.*, 149, 403–424, <https://doi.org/10.1007/s10546-013-9852-8>, 2013.

780
781 Wood, R., Wyant, M., Bretherton, C. S., Rémillard, J., Kollias, P., Fletcher, J., Stemmler, J., De Szoeko, S., Yuter, S., Miller, M.,
782 Mechem, D., Tselioudis, G., Chiu, J. C., Mann, J. A. L., O'Connor, E. J., Hogan, R. J., Dong, X., Miller, M., Ghate, V.,
783 Jefferson, A., Min, Q., Minnis, P., Palikonda, R., Albrecht, B., Luke, E., Hannay, C., and Lin, Y.: Clouds, aerosols, and
784 precipitation in the marine boundary layer: an arm mobile facility deployment, *Bull. Am. Meteorol. Soc.*, 96, 419–440,
785 <https://doi.org/10.1175/BAMS-D-13-00180.1>, 2015.

786
787 Wyngaard, J. C.: Structure of the PBL, in: *Lectures on Air Pollution Modeling*, edited by: Venkatram, A. and Wyngaard, J. C.,
788 American Meteorological Society, Boston, MA, 9–61, https://doi.org/10.1007/978-1-935704-16-4_2, 1988.

789
790 Xia, H., Shentu, G., Shangguan, M., Xia, X., Jia, X., Wang, C., Zhang, J., Pelc, J. S., Fejer, M. M., Zhang, Q., Dou, X., and Pan,
791 J.: Long-range micro-pulse aerosol lidar at 1.5 μm with an upconversion single-photon detector, *Opt. Lett.*, 40, 1579–1582,
792 <https://doi.org/10.1364/OL.40.001579>, 2015.

793
794 Xia, H., Shangguan, M., Wang, C., Shentu, G., Qiu, J., Zhang, Q., Dou, X., and Pan, J.: Micro-pulse upconversion doppler lidar
795 for wind and visibility detection in the atmospheric boundary layer, *Opt. Lett.*, 41, 5218, <https://doi.org/10.1364/ol.41.005218>,
796 2016.

797
798 Xia H., Chen Y., Yuan J., Su L., Yuan Z., Huang S., and Zhao D.: Windshear detection in rain using a 30 km radius coherent doppler
799 wind lidar at mega airport in plateau, *Remote Sens.*, 16, 924, <https://doi.org/10.3390/rs16050924>, 2024.

800
801 Xue, L., Zhou, D., Huang, X., Lou, S., and Ding, A.: Climatological characteristics of cold fronts and their impacts on air quality
802 in cold seasons over the eastern China, *J. Geophys. Res. Atmospheres*, 127, e2022JD037488, <https://doi.org/10.1029/2022JD037488>, 2022.

803
804 Yan, Y., Cai, X., Wang, X., Miao, Y., and Song, Y.: Low-level jet climatology of China derived from long-term radiosonde
805 observations, *J. Geophys. Res. Atmospheres*, 126, e2021JD035323, <https://doi.org/10.1029/2021JD035323>, 2021.

806
807 Yan, Y., Cai, X., Miao, Y., and Yu, M.: Synoptic condition and boundary layer structure regulate PM2.5 pollution in the huaihe
808 river basin, china, *Atmospheric Res.*, 269, 106041, <https://doi.org/10.1016/j.atmosres.2022.106041>, 2022.

809
810 Yang, B., Finn, D., Rich, J., Gao, Z., and Liu, H.: Effects of low-level jets on near-surface turbulence and wind direction changes
811 in the nocturnal boundary layer, *J. Geophys. Res. Atmospheres*, 128, e2022JD037657, <https://doi.org/10.1029/2022JD037657>,
812 2023.

813
814 Yang, K., Cai, W., Huang, G., Hu, K., Ng, B., and Wang, G.: Increased variability of the western pacific subtropical high under
815 greenhouse warming, *Proc. Natl. Acad. Sci.*, 119, e2120335119, <https://doi.org/10.1073/pnas.2120335119>, 2022.

816
817 Yang, Y., Fan, S., Wang, L., Gao, Z., Zhang, Y., Zou, H., Miao, S., Li, Y., Huang, M., Yim, S. H. L., and Lolli, S.: Diurnal evolution
of the wintertime boundary layer in urban beijing, china: insights from doppler lidar and a 325-m meteorological tower,
Remote Sens., 12, 3935, <https://doi.org/10.3390/rs12233935>, 2020.

Yin, J., Gao, C. Y., Hong, J., Gao, Z., Li, Y., Li, X., Fan, S., and Zhu, B.: Surface meteorological conditions and boundary layer
height variations during an air pollution episode in nanjing, china, *J. Geophys. Res. Atmospheres*, 124, 3350–3364,
<https://doi.org/10.1029/2018JD029848>, 2019.

Yuan, J., Xia, H., Wei, T., Wang, L., Yue, B., and Wu, Y.: Identifying cloud, precipitation, windshear, and turbulence by deep
analysis of the power spectrum of coherent doppler wind lidar, *Opt. Express*, 28, 37406, <https://doi.org/10.1364/OE.412809>,
2020.

Yue, M., Wang, M., Guo, J., Zhang, H., Dong, X., and Liu, Y.: Long-term trend comparison of planetary boundary layer height in
observations and CMIP6 models over china, *J. Clim.*, 34, 8237–8256, <https://doi.org/10.1175/JCLI-D-20-1000.1>, 2021.

Zhang, C., Ding, R., Xiao, C., Xu, Y., Cheng, H., Zhu, F., Lei, R., Di, D., Zhao, Q., and Cao, J.: Association between air pollution
and cardiovascular mortality in hefei, china: a time-series analysis, *Environ. Pollut.*, 229, 790–797,
<https://doi.org/10.1016/j.envpol.2017.06.022>, 2017.

Zhang, F., Zhang, Q., Du, Y., and Kong, H.: Characteristics of coastal low-level jets in the bohai sea, china, during the early warm

818 season, *J. Geophys. Res. Atmospheres*, 123, 13,763-13,774, <https://doi.org/10.1029/2018JD029242>, 2018.

819 Zhang, H., Zhang, X., Li, Q., Cai, X., Fan, S., Song, Y., Hu, F., Che, H., Quan, J., Kang, L., and Zhu, T.: Research progress on
820 estimation of the atmospheric boundary layer height, *J. Meteorol. Res.*, 34, 482–498, [https://doi.org/10.1007/s13351-020-](https://doi.org/10.1007/s13351-020-9910-3)
821 [9910-3](https://doi.org/10.1007/s13351-020-9910-3), 2020.

822 Zhang, L., Zhang, H., Li, Q., Wei, W., Cai, X., Song, Y., Mamtimin, A., Wang, M., Yang, F., Wang, Y., and Zhou, C.: Turbulent
823 mechanisms for the deep convective boundary layer in the taklimakan desert, *Geophys. Res. Lett.*, 49, e2022GL099447,
824 <https://doi.org/10.1029/2022GL099447>, 2022.

825 Zhang, Y., Zuo, Q., Wu, Q., Han, C., and Tao, J.: An integrated diagnostic framework for water resource spatial equilibrium
826 considering water-economy-ecology nexus, *J. Clean. Prod.*, 414, 137592, <https://doi.org/10.1016/j.jclepro.2023.137592>, 2023.

827 Zhao, P., Zhang, R., Liu, J., Zhou, X., and He, J.: Onset of southwesterly wind over eastern China and associated atmospheric
828 circulation and rainfall, *Clim. Dyn.*, 28, 797–811, <https://doi.org/10.1007/s00382-006-0212-y>, 2007.

829 Zhao, S., He, J., Dong, L., Qi, S., Yin, D., Chen, J., and Yu, Y.: Contrasting vertical circulation between severe and light air pollution
830 inside a deep basin: results from the collaborative experiment of 3D boundary-layer meteorology and pollution at the sichuan
831 basin (BLMP-SCB), *Bull. Am. Meteorol. Soc.*, 104, E411–E434, <https://doi.org/10.1175/BAMS-D-22-0150.1>, 2023.

832 Zhao, W. and Zou, Y.: Hefei: an emerging city in inland china, *Cities*, 77, 158–169, <https://doi.org/10.1016/j.cities.2018.01.008>,
833 2018.

834 Zhou, J.: Lidar observations of asian dust over hefei, china, in spring 2000, *J. Geophys. Res.*, 107, 4252,
835 <https://doi.org/10.1029/2001JD000802>, 2002.

836 Zhu, F., Ding, R., Lei, R., Cheng, H., Liu, J., Shen, C., Zhang, C., Xu, Y., Xiao, C., Li, X., Zhang, J., and Cao, J.: The short-term
837 effects of air pollution on respiratory diseases and lung cancer mortality in hefei: a time-series analysis, *Respir. Med.*, 146,
838 57–65, <https://doi.org/10.1016/j.rmed.2018.11.019>, 2019.

839